An *in situ* shearing X-ray measurement system for exploring structures and dynamics at the solid-liquid interface

Yijun Qiao,[1,2,3] Hua Zhou,[4] Zhang Jiang,[4] Qiming He,[2,3,5] Shenglong Gan,[2] Hongdong Wang,[1] Shizhu Wen,[1] Juan de Pablo,[2,3,5] Yuhong Liu,[1 c)] Matthew V. Tirrell,[2,3,5 b)] Wei Chen[2,3,5 a)]

[1]State Key Laboratory of Tribology, Tsinghua University, Beijing, 100084, China

[2]Materials Science Division, Argonne National Laboratory, Lemont, IL 60439, USA

[3]Advanced Materials for Energy-Water Systems Center, Argonne National Laboratory, Lemont, IL 60439, USA

[4]X-ray Science Division, Advanced Photon Source, Argonne National Laboratory, Argonne, IL 60439, USA

[5]Pritzker School of Molecular Engineering, University of Chicago, Chicago, IL 60637, USA

Author to whom correspondence should be addressed.

[a)] Electronic mail: wchen@anl.gov

[b)] Electronic mail: mtirrell@anl.gov

[c)] Electronic mail: yuhongliu@tsinghua.edu.cn

ABSTRACT

Revealing interfacial structure and dynamics has been one of the essential thematic topics in material science and condensed matter physics. Synchrotron-based X-ray scattering techniques can deliver unique and insightful probing of interfacial structures and dynamics, in particular in reflection geometries with higher surface and interfacial sensitivity than transmission geometries. We demonstrate the design and implementation of an *in situ* shearing X-ray measurement system, equipped with both inline parallel-plate and cone-and-plate shearing setups and operated at the Advanced Photon Source (APS) at Argonne National Laboratory, to investigate the structures and dynamics of end-tethered polymers at the solid-liquid interface. With a precise lifting motor, a micrometer-scale gap can be produced by aligning two surfaces of a rotating upper shaft and a lower sample substrate. A torsional shear flow forms in the gap and applies tangential shear forces on the sample surface. The technical combination with nanoscale rheology and the utilization of *in situ* X-ray scattering allow us to gain fundamental insights into the complex dynamics in soft interfaces under shearing. In this work, we demonstrate the technical scope and experimental capability of the *in situ* shearing X-ray system through the measurements of charged polymers at both flat and curved interfaces upon shearing. Through the *in situ* shearing X-ray scattering experiments integrated with theoretical simulations, we aim to develop a detailed understanding of the short-range molecular structure and mesoscale ionic aggregate morphology, as well as ion transport and dynamics in soft interfaces, thereby providing fundamental insight into a long-standing challenge in ionic polymer brushes with significant technological impact.

I. INTRODUCTION

Interface engineering has become increasingly critical for the development of tribology,[1] biology,[2] and microelectronics.[3] The structures and physical properties of materials at interfaces are different from those in bulk, leading to many intriguing

phenomena and novel functionalities, such as the density oscillation of water at the hydrophilic mica surface,[4] the depletion of water at the hydrophobic surface,[5] a highly conducting and even superconducting layer at the heterointerface of two insulating oxides,[6] and so on. In soft materials, many technical applications rely on the strong response of soft interfaces to rather weak forces; and the properties of such a soft interface could be switched by weak external stimuli. For example, a unique type of responsive soft interface is created by polymer brushes consisted of densely tethered, long polymer chains at its solid-liquid interface.[7] Charged polyelectrolyte brushes swell in good solvents such as water but collapse in poor organic solvents.[8] Moreover, polyelectrolyte brushes shrink with increasing salt concentration due to electrostatic screening (polyelectrolyte effect).[8,9] Considerable efforts have been made to decipher the structures and dynamics of polymer brushes upon exposure to various external fields, including exposure to solvents,[8] salts,[9] temperature,[10] pH,[11] magnetic fields,[12]electric fields,[13] and shear force.[14] Among the above stimuli, shear force is very important in the fields of lubrications,[15] water treatment,[16] biological engineering,[2] and battery safety.[17] Knowledge of the response to shearing of polymer brushes, as well as the structural dynamics of polymer brushes, is very incomplete. Consequently, detailed observation and interpretation are required to reach a comprehensive understanding of the structure-property relationship of polymer brushes under shearing processes.

It remains challenging to achieve real-time probing of the structural evolution and dynamics in soft interfaces under shearing processes. Numerous simulations and theoretical methods have been applied, but researchers have drawn opposite conclusions —for both swelling[18,19] and collapse[20–22] — concerning the behavior of polymer brushes under shearing. More persuasive evidence from experiments is required to depict the detail of the molecular behavior and structural dynamics. Some *ex situ* methods have been applied in attempts to indirectly evaluate the tilting behavior or interfacial hydration structure of polymer brushes under shear flow[2] or friction with a ball-and-disk geometry,[15] by evaluating the antifouling performance or friction coefficient of a polymer surface. These efforts were followed by *in situ* characterizations of interfacial polymer brushes under shearing performed using atomic force microscopy[23] or via the surface forces apparatus[24,25] to deduce the structural variation by physical force information. Furthermore, infrared vibrational microscopy[26,27] and photoluminescence spectra[28] have been combined with the ball-and-disk geometry and surface forces apparatus, respectively, to provide direct, real-time chemical information about molecular conformation and polymer chain orientation under shearing. However, obtaining intrinsic information from the interfacial molecules remains beyond our capabilities. With the development of a high-energy synchrotron light source, X-ray reflectivity (XRR)[29–31] has been a promising method to detect the buried nanoscale-interfacial-structure and shear response of soft materials.

In this work, an *in situ* shearing X-ray measurement system equipped with parallel-plate and cone-and-plate shearing setups has been designed and implemented at the Advanced Photon Source (APS) at Argonne National Laboratory. Aiming to test the feasibility of our *in situ* measurement system and study the structural dynamics of polymer brushes at the solid-liquid interface, we

measured the X-ray scattering of charged polymers at both flat interfaces and curved interfaces under diverse shearing conditions. Next, we compared the swelling behaviors between amino acid-based poly(acetylcysteine methacrylate) (PACysMA) and poly(cysteine methacrylate) (PCysMA) brushes on silicon substrates and demonstrated the significant influence of electrostatic interactions on the shear response of polymer brushes. In addition, we evaluated the interparticle interactions of polyzwitterionic poly(2-methacryloyloxyethyl phosphorylcholine) (PMPC) brushes grafted on silicon dioxide (SiO_2) nanospheres (SiO_2-PMPC), which revealed a uniform distribution but a less aggregated status under shearing. The successful application of the *in situ* shearing X-ray measurement system provides an extra view to gain insights into the dynamics in soft interfaces under shearing processes.

II. TECHNICAL DESIGN AND ALIGNMENT

Shown in Fig. 1 is the schematic diagram of our *in situ* shearing X-ray measurement system commissioned at beamline 12-ID-D at the APS. A focused monochromatic X-ray beam with a micron-scale beam profile is delivered to the experimental hutch by the primary beamline component consisting of undulator, horizontal mirror, monochromator, compound refractive lens, filter, and slit. Samples are placed in the shearing setup as shown in Fig. 1(b), and the diffraction patterns are collected by an X-ray photon counting area detector (Dectris, Pilatus-100K). The spatial positions of shearing

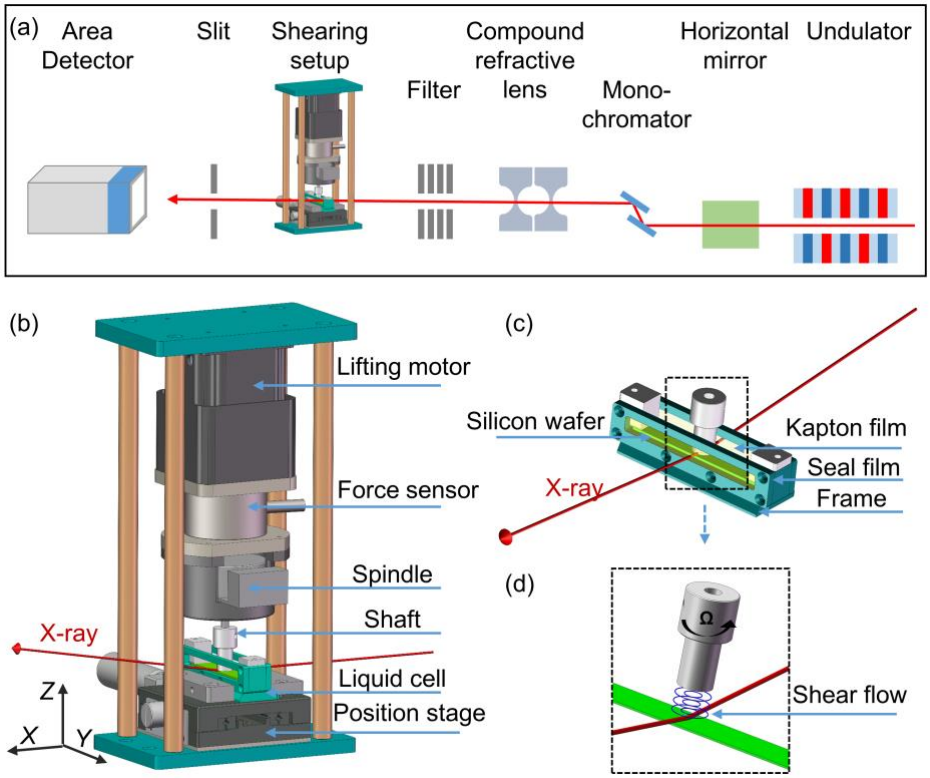

FIG. 1. (a) Schematic diagram of the *in situ* shearing X-ray measurement system; (b) a three-dimensional (3D) model of the shearing setup equipped with a movable liquid cell; (c) detail of the liquid cell; and (d) schematic shear flow in a micrometer-scale gap in the parallel-plate or cone-and-plate shearing measurement system.

setup and detector can be adjusted by a five-circle diffractometer served at beamline 12-ID-D. A replaceable shaft and liquid cell are two key parts to constructing the parallel-plate or cone-and-plate shearing measurement system. The focused X-ray beam passes through the gap between the shaft and the bottom substrate surface in the liquid cell. The shearing measurements may be performed by either immersing the shaft and the substrate in liquids or filling the gap between the shaft and the substrate with liquids. The position stage is used to transform the substrate perpendicular to the direction of the X-ray beam (along the *Y* axis in Fig. 1(b)).

To perform surface X-ray scattering experiments in a liquid environment and under shearing, single-crystal silicon substrates are used as the bottom substrate in the liquid cell because they are uniformly flat and thus make it easy to perform the surface functionalization to create the desired soft interfaces. Silicon substrates are fixed at the bottom of the liquid cell via two Teflon clamps. In this setup, the potential deformation of silicon substrates arising from Teflon clamps is negligible as evidenced by X-ray scans. To prevent liquid corrosion and impurity introduction, the main frames of the liquid cell made of stainless steel are passivated by immersing stainless-steel parts into 30% nitric acid (HNO_3) at 60°C for 30 minutes and then rinsing with deionized water to remove excess acids. The inner width of the liquid cell is 10 mm. At the photon energy of 20 keV, 49.6% of the X-ray beam could transmit through the 10-mm liquid layer above the substrate. The depth of the cell is 10 mm to keep the shaft as short as possible and thus reduce the face runout upon rotating. Two Kapton windows, which have uniform electron density and smooth surfaces to avoid X-ray wavefront disturbance at the small-angle regime,[32] are installed on both sides of the liquid cell. Teflon sealing films between the Kapton window and the stainless-steel frame are used to prevent leakage of electrolytes.

Precise alignment of the end surface of parallel-plate shaft with the silicon substrate in the liquid cell creates a micron-scale gap. The measured face runout in the *X*-*Y* plane (Fig. 1(b)) of the plane-shaft with an 8-mm diameter is around 1 μm. The lifting motor with a resolution of 0.1 μm is responsible for the vertical motion of the shaft and the gap size alignment, with the help of a force sensor that has a resolution of 0.01 N. Prior to the gap size alignment, the zero-gap position is determined and calibrated as follows: at first, keep a non-contact status between the shaft and substrate and set the parameter of force sensor as zero. Then, move the shaft toward the substrate until a critical contact force of 0.10 N is reached. Last, withdraw the shaft and set the position where the contact force returns to 0.00 N as the zero-gap position. The gap size is set to be 140 μm to avoid blocking the X-ray beam with a vertical size of 76 μm.

For the cone-and-plate geometry, as shown in Fig. S1 in Supporting Information, a truncated plateau at the cone tip is made to avoid blocking the X-ray beam in a grazing incident angle of less than or equal to 1.5°. The cone angle is 4° to maximize the shear rate of the geometry and decrease the plateau diameter. The calibration procedures of the cone-and-plate measurement system are identical to those of the parallel-plate system. In contrast to the coaxial cylinder geometry[33,34] and fluid channel geometry[33,35–37] widely used in neutron reflectivity, our parallel-plate and cone-and-plate shearing setups are more suitable for *in situ* XRR measurement and thus can render a

high-resolution electron density profile at the solid-liquid interfaces. The plate geometries also eliminate the substrate deformation[38] and structural dynamics from the increased liquid pressure[39] in fluid channel geometry. One of the advantages of the cone-and-plate measurement system is the uniform shear rate in the gap, which depends only on cone angle and angular velocity.

Before each X-ray experiment, the entire setup is aligned by a four-circle diffractometer to make sure the substrate is parallel to the X-ray beam. A gap with a size of tens of micrometers is applied in experiments. Uniform shear flow in the micrometer-scale-gap is formed by rotating the shaft in an angular velocity, Ω, as shown in Fig. 1(d).

III. FLOW FIELD ANALYSIS

A stable shear flow field is necessary for the study on interfacial structures under shearing. A Reynolds number (*Re*) is usually used to evaluate the status of a liquid flow. For a geometry with a rotating plate immersed in a liquid cell, a rotational Reynolds number[40] is given by

$$Re = \frac{\rho N D^2}{\mu} \quad (1),$$

where ρ is the density of the liquid, μ is the dynamic viscosity, N is the angular velocity in rad per second, and D is the diameter of the shaft. For a parallel-plate geometry, the gap ratio (the ratio between the gap size and the radius of the shaft) and *Re* codetermine the flow condition.[41] For the shearing setup, the radius of the shaft is 4 mm, and the gap

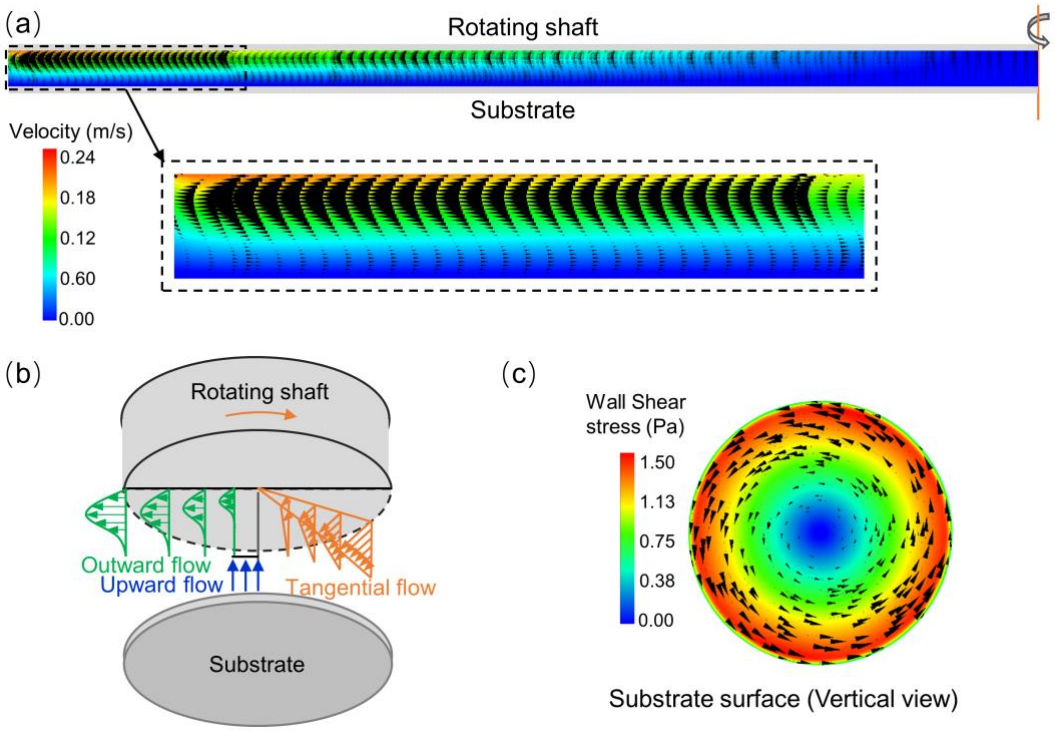

FIG. 2. A computational fluid dynamics (CFD) simulation of the flow field in the *X*-*Z* plane in Fig. 1(b) in the parallel-plate geometry. (a) The velocity field in the section of the 140-μm gap. The colormap represents the velocity value, and the black arrows represent the in-plane velocity direction. An enlarged view is given in the dash box. (b) A schematic of the flow in the gap of the parallel plates. The tangential flow, outward flow, and upward flow are marked by orange, green, and blue arrows. (c) The flow field at the surface of the silicon substrate. The colormap represents the shear stress. The black arrows represent the in-plane velocity direction.

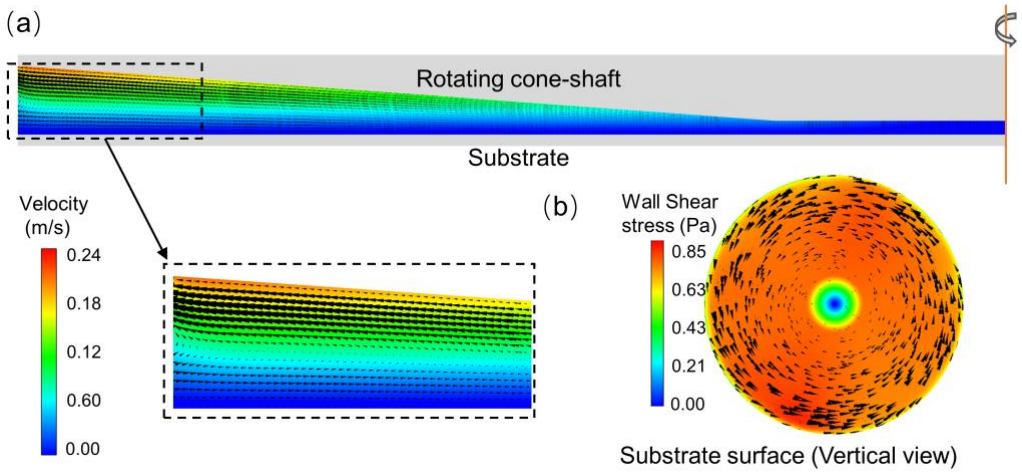

FIG. 3. A CFD simulation of the flow field in the *X-Z* plane in Fig. 1(b) in the cone-plate geometry. (a) The velocity field in the section of the gap. The colormap represents the velocity value, and the black arrows represent the in-plane velocity direction. An enlarged view is given in the dash box. (b) The flow field at the surface of the silicon substrate. The colormap represents the shear stress. The black arrows represent the in-plane velocity direction.

size is 140 μm. Laminar flow is formed with a gap ratio of 0.035 and *Re* lower than 10,000 (corresponding to a rotating speed of 1500 rpm). A laminar flow condition is ensured by adopting a relatively low rotating speed of 500 rpm.

The tangential shear rate[42] of the parallel-plate geometry is given by

$$\dot{\gamma} = \frac{V}{h} \qquad (2),$$

where V is the tangential velocity and h is the gap size. Since the shear rate of the parallel-plate geometry depends on the velocity and radius, a nominal shear rate at the rim of the plate[43] is used in the following description of parallel-plate measurements. Smaller gap size and higher rotational speed result in higher shear rate.

For the cone-and-plate geometry, the tangential shear rate in the gap is uniform and is given by

$$\dot{\gamma} = \frac{\Omega}{\theta} \qquad (3),$$

where Ω is the angular velocity in rad per second and θ is the cone angle.

We performed a dynamic simulation of the flow using ANSYS Fluent to obtain an insight into the flow condition in the liquid cell. A laminar flow model and a Rotating Reference Frame Model are applied in the simulation. Water is applied as the fluid. For the parallel-plate geometry, the gap between the shaft and substrate surface is 140 μm, and the rotation speed of the shaft is 500 rpm. Fig. 2(a) shows a section of the CFD results from the velocity field in the *X-Z* plane in Fig. 1(b). An enlarged view of the velocity field in the gap is given in the dashed box to emphasize the flow direction. As shown by the black arrows, the liquid near the upper rotating shaft tends to flow from the center of the gap to the edge of the shaft, that is, as a radial outward flow. The liquid near the lower static substrate flows radially inward. To maintain the flow continuity, there exists an upward flow at the center of the gap, comparable to the downward flow in Garrett's research on a rotating system consisting of an upper static plane and a lower rotating plane.[44] The formation of the outward flow is ascribed to the centrifugal force,[44,45] which drives a radially outward flow and, in turn, leads to an upward flow at the rotating center. A schematic of the flow

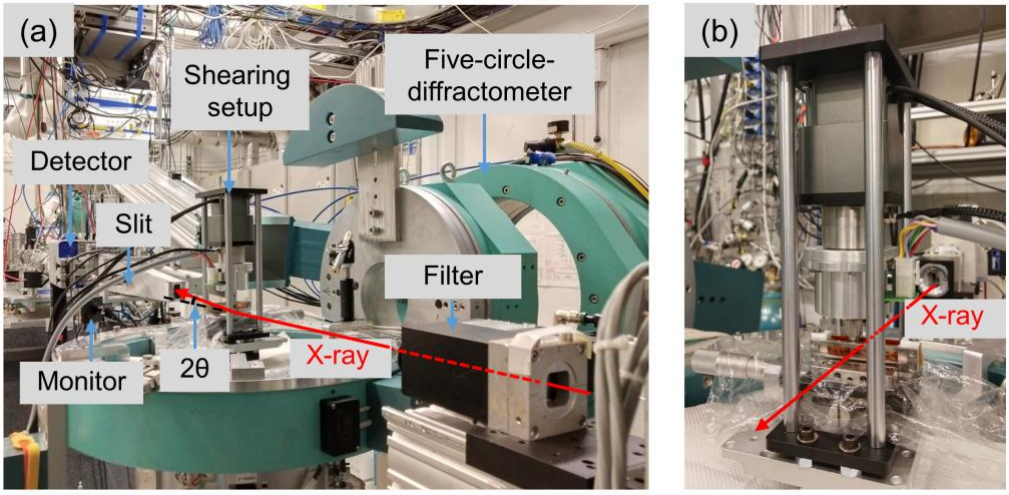

FIG. 4. (a) The *in situ* shearing X-ray measurement system is set up at APS beamline 12-ID-D; and (b) a real-time image from an inline video camera shows the status of the shearing setup.

near the rotating shaft is given in Fig. 2(b). Under the no-slip condition, the boundary layer of liquids near the rotating plane is driven to form an azimuthal and tangential flow. Fig. 2(c) depicts the in-plane flow at the substrate surface (black arrows) and the resulting wall shear stress (colormap). The wall shear stress is the product of the shear rate and the dynamic viscosity of water. The distribution of the shear stress is inhomogeneous, depending on the radius of the shaft.

In the cone-and-plate geometry, a similar radial outward flow near the rotating shaft is also obtained, as indicated by the black arrows in the CFD simulation (Fig. 3(a)); however, the shear stress generated by the shear flow on the substrate surface is uniform except in the center region, as shown by the colormap in Fig. 3(b). Given the existence of a plateau at the top of the conical shaft, the low shear stress region appears (Fig. S1).

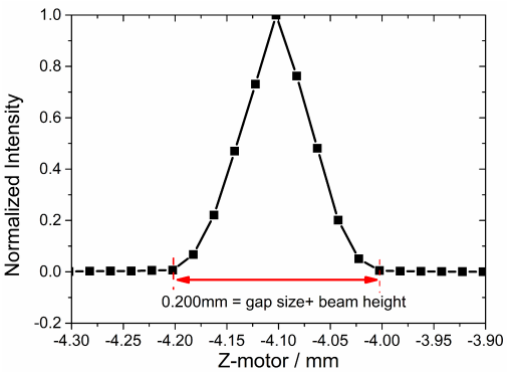

FIG. 5. The gap size verified by a Z-axis scan of the X-ray beam with a vertical size of 76 μm.

IV. PRELIMINARY EXPERIMENTS

Preliminary *in situ* X-ray measurements on two different types of end-tethered polymer brushes, which are grafted on either the flat silicon wafer or silica nanospheres, have been performed with the parallel-plate shearing measurement system (Fig. 4).

A. X-RAY REFLECTIVITY

XRR on a flat silicon wafer has been carried out at 20.0 keV with a beam size of 150 μm × 76 μm (horizontal versus vertical) at beamline 12-ID-D at the APS. Low divergence in both horizontal and vertical directions provides XRR measurements with a sufficiently high resolution in q-space. A Pilatus 100K area detector was mounted on the diffractometer arm to collect the data. After the zero-gap calibration, the gap was set to be 140 μm, in which the shaft would not block the X-ray beam in the entire range of scattering angle 2θ up to 3°. The gap size has also been verified by a Z-height scan of

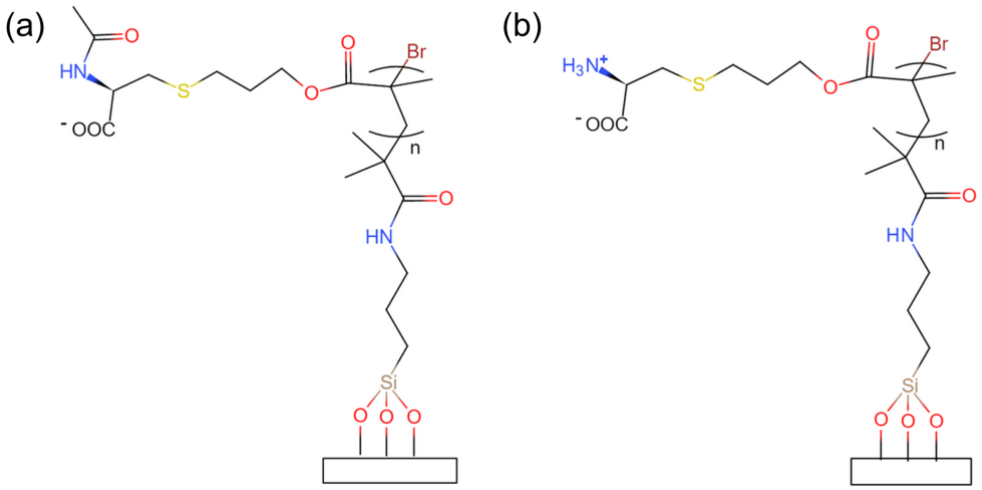

FIG. 6. The chemical structure of (a) PACysMA and (b) PCysMA.

the X-ray beam. In Fig. 5, the intensity first increases and then decreases when the entire setup is lifted by the Z-motor of the five-circle diffractometer, indicating that the beam passes the gap. The width of the intensity peak, 200 μm, is a sum of the gap size and beam height. Thus, the measured gap size is 124 μm. Given that the resolution of the Z-axis scan is 20.0 μm, the measured gap size matches well with the preset value.

Two kinds of polymer brushes, PACysMA and PCysMA, with high grafting density (≈ 0.1 chains/nm^{-2}) are synthesized on silicon wafers (55 × 10 × 0.5 mm). A detailed description of their synthesis is given in the Supporting Information. Both PACysMA and PCysMA have identical main chain structures, but negative charges and polyzwitterions on their side chains, respectively (Fig. 6). The experimental procedure is as follows: First, we mounted the brush sample into the liquid cell without adding water. Second, we performed the calibration and set the gap size to 140 μm. Third, we collected XRR data on dry brush films. Fourth, we measured XRR on different polymer brushes under static water and under shear rates of 150 and 1500 s^{-1}. Each measurement was taken after an equilibrium time of 15 minutes. Because the beam width was 150 μm, four XRR measurements for each brush sample were performed step by step at the horizontal center of the gap within a range of 600 μm. The deviation of shear rates due to radius offsets is negligible. In Fig. S2, XRR profiles of both the PACysMA and PCysMA dry brush films exhibit smooth interference fringes, indicating a sharp brush-air interface and good film quality.

Fig. 7 shows the raw XRR profiles of the PACysMA and PCysMA brushes in static water and shear flows and their corresponding best-fits using a generalized skew-symmetric probability density function.[46] The XRR profiles in the insets are plotted as Iq^4 vs. q to highlight the variations under different shearing conditions. For PACysMA (the inset of Fig. 7(a)), XRR fringes are shifted to a lower q region and their width decreases, suggesting that the brush layer thickness increases upon shearing in contrast to that in static water. The increase of peak intensity of the fringe around 0.10 Å^{-1} and the generation of a new fringe around 0.19 Å^{-1} indicate a sharper brush-liquid interface under shearing. The intensities around 0.19 Å^{-1} increase with shear rates, indicating a stronger interface sharpening effect upon shearing. For PCysMA (the inset in Fig. 7(c)), only an

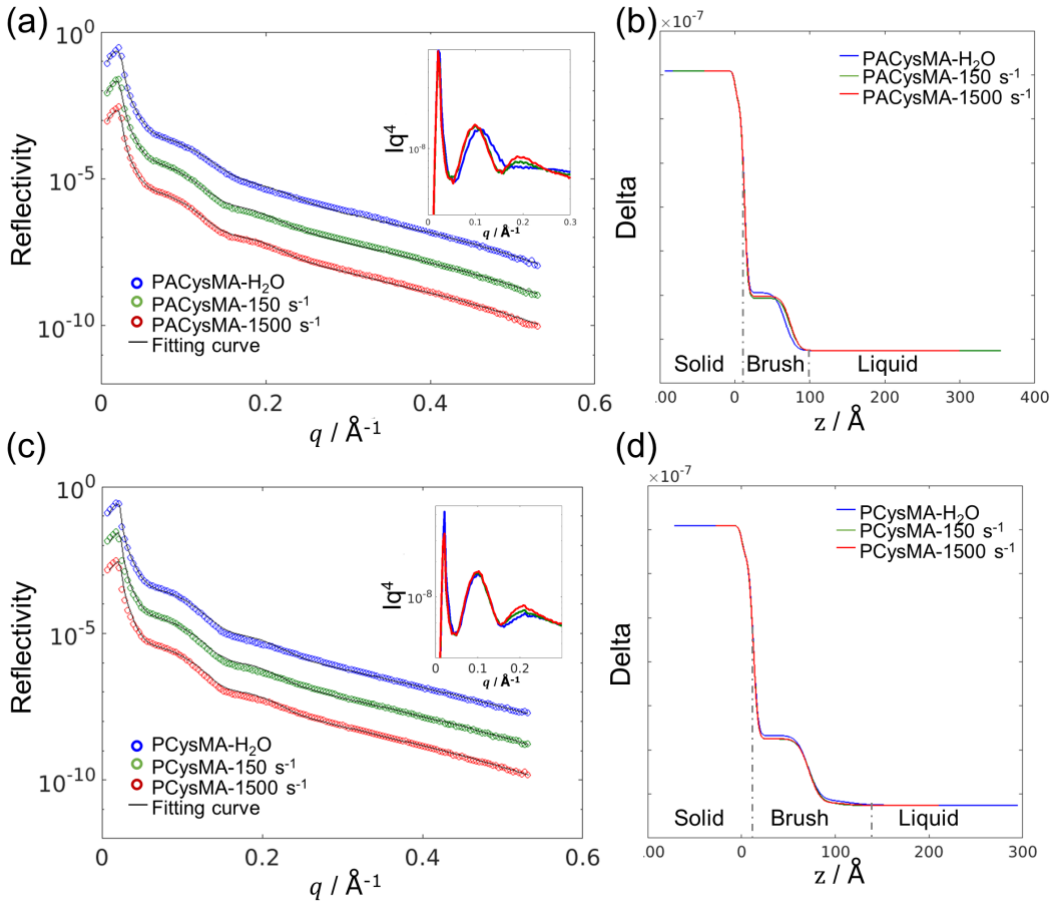

FIG. 7. The XRR and fitting data of (a) PACysMA and (c) PCysMA under static water (blue line) and shear rates of 150 s^{-1} (green line) and 1500 s^{-1} (red line); raw XRR data are shown in the insets. (b) and (d) show the density profile from the fitting data.

increase of the fringe intensity around 0.21 $Å^{-1}$ is observed, indicating an interface sharpening effect but no swelling effect under shearing.

For further analysis, the reflectivity data were fitted to extract their corresponding electron density profiles. For PACysMA in Fig. 7(b), the height changes in the density profile revealed that the thickness increases under shearing, which matches well with the feature of the XRR fringes. For PCysMA, the length of the brush region remains constant under shearing, indicating an unchanged layer thickness. However, the decrease in the height of the density profile still indicates a variation of internal brush structures.

Understanding the molecular behavior and dynamics of polymer brushes under shearing is essential in the fields of polymer science and tribology. From results from most of the *in situ* X-ray or neutron experiments, the vertical density profiles of the polymer brushes under shearing remained unchanged and the thickness decreased because of wiping off the stimuli or desorption.[35,36,47,48] However, Kelin *et al.*[49] showed an increase of up to 20% in brush thickness resulting from the shear flow by surface force apparatus. Kumaran *et al.*[49] also supported the thickness swelling effect under shear flow by theoretical analysis. The increasing effect occurs because of a net upward force from the hydrodynamic effect when a tangential shear force was applied at the surface of the brush. Barrat *et al.*[49] predicted an increase in the brush thickness

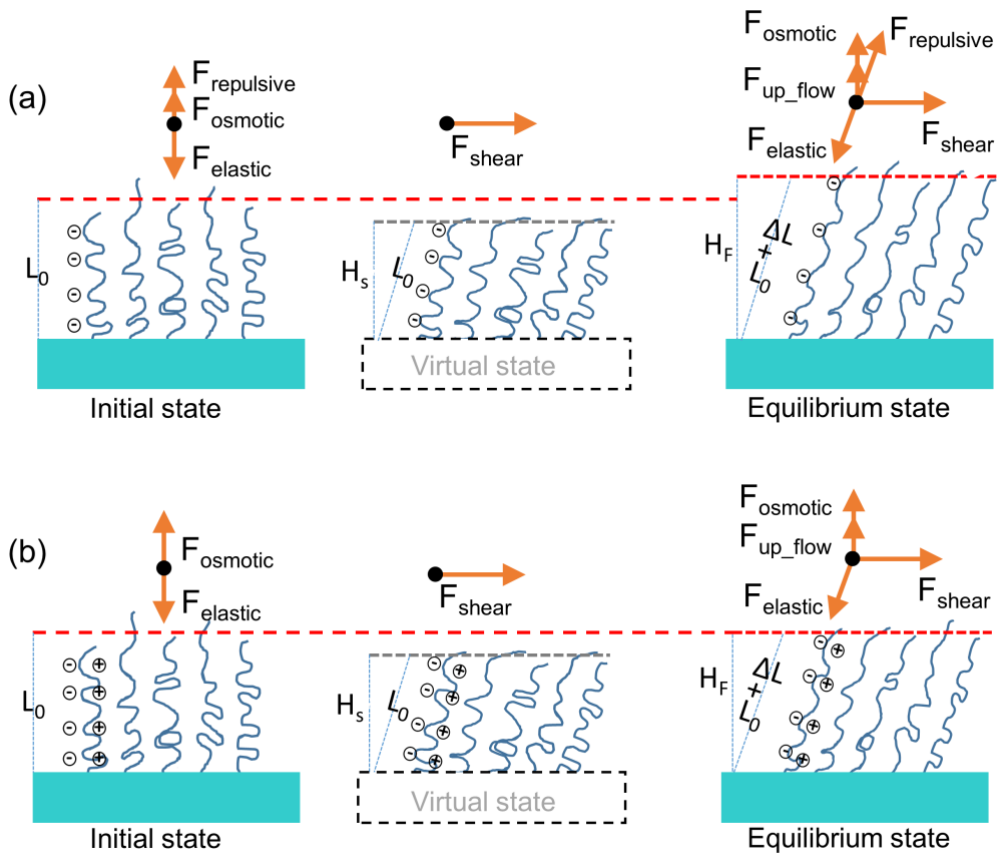

FIG. 8. Schematic of the structure dynamics of (a) PACysMA and (b) PCysMA under shearing.

as a result of the decrease in the osmotic compressibility due to the tangential shear force at the free surface. Nevertheless, this demonstration is the first time that the swelling effect of the polymer brushes under shearing has been observed by *in situ* X-ray reflectivity.

Herein we propose a model to explain the structure and dynamics under shearing by including the tangential shear stress, upward flow, and electrostatic interaction. As shown in Fig. 8(a), in the initial static state, the PACysMA brush stretches into water and reaches a stable condition under a balance of elastic force (deformation of molecular backbone), osmotic pressure (interactions between monomers), and electrostatic repulsion (negative charges at a carboxylic group). The length difference between each polymer chain is the main reason for the interface roughness. Tangential shear flow and upward flow are simultaneously formed by our shearing setup. A virtual state is hypothesized to describe the effect of tangential shear force. It is known that the polymer chains tilt under shearing, which should result in a thinner layer and a smaller interfacial roughness. For the equilibrium state, a vertical shear stress from the upward flow is considered. The PACysMA brush layer reaches a greater thickness than that in its initial state under a balance of osmotic pressure, electrostatic repulsion, upward flow shear stress, elastic tension, and tangential shear force. For PCysMA in Fig. 8(b), the main difference is the lack of electrostatic repulsion, as compared with PACysMA. The result reveals that the electrostatic interaction significantly influences the interfacial polymer brush

structure under shear flow. It has been proved that polymer brushes with greater thickness exhibited a better lubricity[50,51]. Here, the swelling effect of the PACysMA brush under shearing may also result in a lower friction coefficient and better lubrication.

In summary, by comparing the shear responses of different polymer brushes, the interfacial molecular behaviors can be distinguished, and the mechanism can be revealed by our *in situ* shearing X-ray measurement system (more detailed studies on the shearing effects will be discussed in the future work).

B. SMALL-ANGLE X-RAY SCATTERING

Grazing incidence small-angle X-ray scattering (GISAXS, reflection geometry) and small-angle X-ray scattering (SAXS, transmission geometry) performed on a polymer brush grafted onto a curved interface have been carried out at beamline 8-ID-E at the APS, as shown in Fig. 9(a). The photon energy is set to 10.92 keV, and the beam size is focused to 100 μm × 10 μm (horizontal versus vertical). PMPC grafted on SiO_2 nanospheres (to create SiO_2-PMPC has been used in this experiment. The synthesis of SiO_2-PMPC is introduced in Supporting Information. The SiO_2-PMPC aqueous solution with a concentration of 20wt% had been prepared, and 5 μL of the solution was dropped into the center of the silicon substrate by using a pipette. The gap

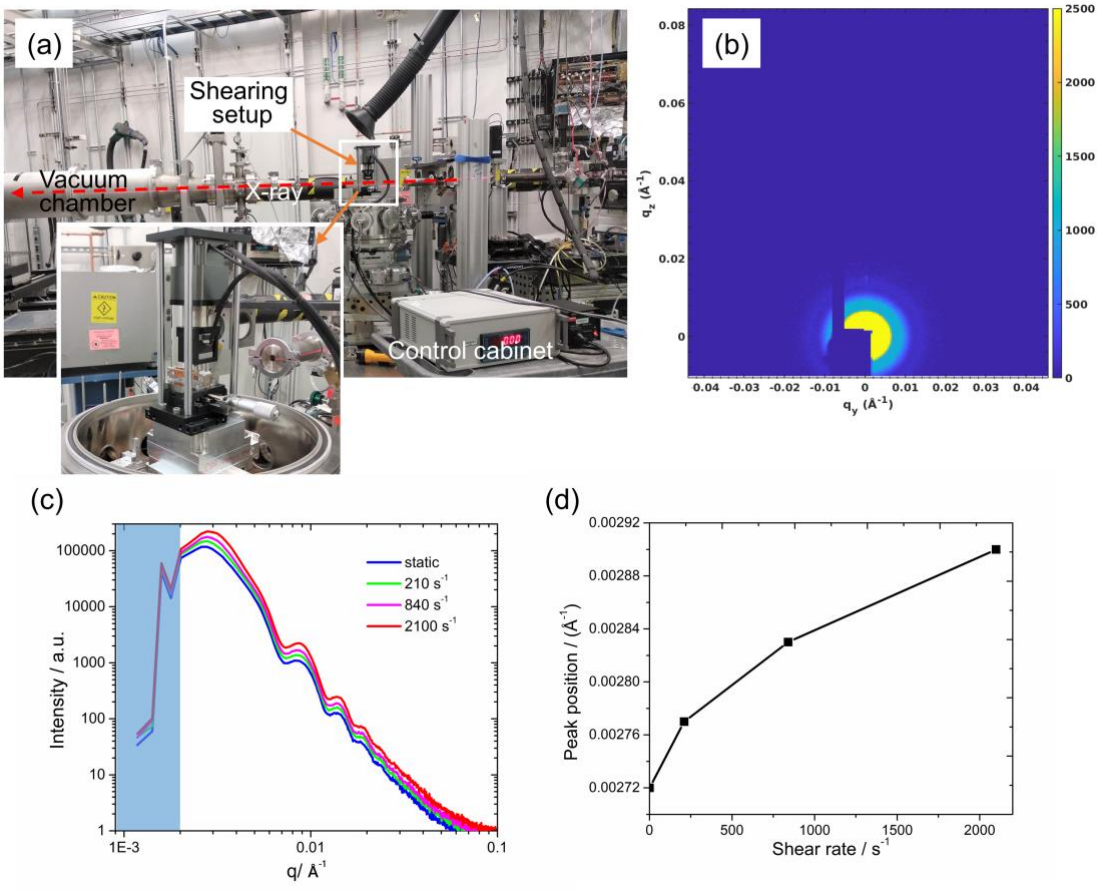

FIG. 9. (a) The *in situ* shearing X-ray measurement system at beamline 8-ID-E. The inset is an enlarged view of the shearing setup. (b) A 2D SAXS pattern of SiO_2-PMPC nanospheres. (c) The angular integration of a line cut of scattering patterns under different conditions (the shield area indicates the X-ray beam stop region). (d) The shift of the peak position under shearing.

between the shaft and silicon substrate was set to be 100 μm, which was filled by the SiO_2-PMPC aqueous solution only. In such a parallel-plate geometry with the gap filled by liquid, flow instability may occur under excessive shear rate owing to the large centrifugal forces. A critical shear rate[43] is given by

$$\dot{\gamma}_c = \frac{1}{h}\sqrt{\frac{20\sigma}{3\rho h}} \quad (4),$$

where ρ is the density, σ is the surface tension, and h is the gap size. For water in the working gap of 100 μm used in our measurements, the critical shear rate is 2.2×10^4 s^{-1}, which corresponds to a rotating speed of 5259 rpm. For the small-angle X-ray experiments, a maximum shear rate of 2.1×10^3 s^{-1} (500 rpm) is applied to ensure a stable and laminar flow condition.

The results using GISAXS under different shear conditions have no change, and thus are not presented here. For SAXS measurements, the X-ray beams go through the center of the gap between the shaft and substrate. The distribution of the SiO_2-PMPC nanospheres and intermolecular interaction are revealed by SAXS. As shown in Fig. 9(b), the SAXS pattern of the static SiO_2-PMPC solution is a uniform ring, indicating an isotropic distribution of the SiO_2-PMPC nanospheres. The shape of the ring remains isotropic while the intensity and peak position of the ring varies under shearing. The angular integration of the line cut of the scattering pattern is shown in Fig. 9(c), which indicates that the intensity of the scattering increases with shear rate. The first structure factor peak near 0.0028 A^{-1} is usually used to analyze the interaction between nanospheres. The shift of the peak position was shown in Fig. 9(d). With the shear rate increasing, the peak shifts to a higher q position, indicating that SiO_2-PMPC nanospheres become less aggregated in a semidilute solution under shearing. The above results confirm the ability of the *in situ* shearing X-ray measurement system to be used for study on the soft interface of a specially shaped surface.

V. CONCLUSIONS

The *in situ* shearing X-ray measurement system has been successfully built and tested. This instrument can be utilized for the study on the structure and dynamics of polymer brushes and nanospheres under shearing at the solid-liquid interface. A phenomenon of the thickness swelling effect of the interfacial PACysMA polymer brush under shearing has been observed for the first time by X-ray reflectivity, a finding that is consistent with some previously theoretical and experimental reports on polymer brushes. The vertical shear stress from an upward flow and the electrostatic interaction between monomers have been considered to be the main reasons for the thickness swelling effect. The instrument has also been used to study the interactions between SiO_2-PMPC nanospheres under shearing. Through concerted theoretical simulations and *in situ* shearing X-ray scattering experiments, we will be able to deliver detailed understanding of molecular conformation and mesoscale ionic aggregate morphology, as well as ion transport and dynamics in soft interfaces, deciphering the mechanism underlying some important interfacial phenomena under shearing.

V. SUPPORTING INFORMATION

See Supporting Information for the synthesis of the polymer brushes, the schematic of the cone-and-plate geometry, and the XRR of dry polymer brushes on a silicon substrate.

VI. ACKNOWLEDGMENTS

Work in the Materials Science Division of Argonne National Laboratory (Conceptual

design and testing, data collection and analysis), was supported by the U.S. Department of Energy, Office of Science, Office of Basic Energy Sciences, Materials Science and Engineering Division. The synthetic work of PACysMA and PCysMA polymer brushes was supported as part of the Advanced Materials for Energy-Water Systems (AMEWS), an Energy Frontier Research Center funded by the U.S. Department of Energy, Office of Science, Basic Energy Sciences. Work by H. Wang, S. Wen and Y. Liu (fabrication of *in situ* shearing X-ray measurement system) was supported by Natural Science Foundation of China (No. 51875303). This research used resources of the Advanced Photon Source (APS) and the Center for Nanoscale Materials (CNM), two U.S. Department of Energy (DOE) Office of Science User Facilities operated for the DOE Office of Science by Argonne National Laboratory under Contract No. DE-AC02-06CH11357. In addition, we gratefully acknowledge the computing resources provided on Bebop, a high-performance computing cluster operated by the Laboratory Computing Resource Center at Argonne National Laboratory.

REFERENCES

1. J. Li and J. Luo, Langmuir **33**, 12596 (2017).
2. K. Yu, P. Andruschak, H. H. Yeh, D. Grecov, and J. N. Kizhakkedathu, Biomaterials **166**, 79 (2018).
3. P. Maheshwari, S. Mukherjee, D. Bhattacharya, S. Sen, R. B. Tokas, and Y. Honda, et al., ACS Appl. Mater. Inter. **7**, 10169 (2015).
4. L. Cheng, P. Fenter, K. L. Nagy, M. L. Schlegel, and N. C. Sturchio, Phys. Rev. Lett. **87**, 156103 (2001).
5. S. Chattopadhyay, A. Uysal, B. Stripe, Y. Ha, T. J. Marks, and E. A. Karapetrova, et al., Phys. Rev. Lett. **105**, (2010).
6. H. Y. Hwang, Y. Iwasa, M. Kawasaki, B. Keimer, N. Nagaosa, and Y. Tokura, Nat. Mater. **11**, 103 (2012).
7. B. Zhao and W. J. Brittain, Prog. Polym. Sci. **25**, 677 (2000).
8. T. Wang, Y. Long, L. Liu, X. Wang, V. S. J. Craig, and G. Zhang, et al., Langmuir. **30**, 12850 (2014).
9. J. Yu, J. Mao, G. Yuan, S. Satija, Z. Jiang, and W. Chen, et al., Macromolecules **49**, 5609 (2016).
10. P. Zhuang, A. Dirani, K. Glinel, and A. M. Jonas, Langmuir **32**, 3433 (2016).
11. G. Kocak, C. Tuncer, and V. Butun, Polym. Chem-UK. **8**, 144 (2017).
12. Y. Xu, J. Yuan, B. Fang, M. Drechsler, M. Müllner, and S. Bolisetty, et al., Adv. Funct. Mater. **20**, 4182 (2010).
13. H. Ouyang, Z. Xia, and J. Zhe, Nanotechnology. **20**, 195703 (2009).
14. A. Korolkovas, C. Rodriguez-Emmenegger, A. de Los Santos Pereira, A. Chennevière, F. Restagno, and M. Wolff, et al., Macromolecules **50**, 1215 (2017).
15. Y. Liu, Y. Xiao, and J. Luo, Science China Technological Sciences **55**, 3352 (2012).
16. A. Farrukh, A. Akram, A. Ghaffar, S. Hanif, A. Hamid, and H. Duran, et al., Applied Materials & Interfaces **5**, 3784 (2013).
17. B. H. Shen, B. L. Armstrong, M. Doucet, L. Heroux, J. F. Browning, and M. Agamalian, et al., ACS Appl. Mater. Inter. **10**, 9424 (2018).

18. J. L. Barrat, Macromolecules **25**, 832 (1992).
19. V. Kumaran, Macromolecules **26**, 2464 (1993).
20. M. Deng, X. Li, H. Liang, B. Caswell, and G. E. Karniadakis, J. Fluid Mech. **711**, 192 (2012).
21. P. S. Doyle, E. S. G. Shaqfeh, and A. P. Gast, Phys. Rev. Lett. **78**, 1182 (1997).
22. M. G. Saphiannikova, V. A. Pryamitsyn, and T. Cosgrove, Macromolecules **31**, 6662 (1998).
23. M. Kobayashi, H. Yamaguchi, Y. Terayama, Z. Wang, K. Ishihara, and M. Hino, et al., Macromolecular Symposia **279**, 79 (2009).
24. L. Chai and J. Klein, Macromolecules **41**, 1831 (2008).
25. B. G. P. van Ravensteijn, R. Bou Zerdan, D. Seo, N. Cadirov, T. Watanabe, and J. A. Gerbec, et al., ACS Appl. Mater. Inter. **11**, 1363 (2018).
26. P. M. Cann and H. A. Spikes, Tribol. Lett. **19**, 289 (2005).
27. P. M. Cann, MRS Bull. **33**, 1151 (2008).
28. S. C. Bae, Z. Lin, and S. Granick, Macromolecules **38**, 9275 (2005).
29. C. Yu, G. Evmenenko, J. Kmetko, and P. Dutta, Langmuir **19**, 9558 (2003).
30. C. J. Yu, A. G. Richter, A. Datta, M. K. Durbin, and P. Dutta, Phys. Rev. Lett. **82**, 2326 (1999).
31. G. Renaud, R. Lazzari, and F. Leroy, Surf. Sci. Rep. **64**, 255 (2009).
32. G. Ju, M. J. Highland, C. Thompson, J. A. Eastman, P. H. Fuoss, and H. Zhou, et al., J. Synchrotron Radiat. **25**, 1036 (2018).
33. S. M. Baker, G. Smith, R. Pynn, P. Butler, J. Hayter, and W. Hamilton, et al., Rev. Sci. Instrum. **65**, 412 (1994).
34. J. K. G. Dhont, M. P. Lettinga, Z. Dogic, T. A. J. Lenstra, H. Wang, and S. Rathgeber, et al., Faraday Discuss. **123**, 157 (2003).
35. D. van der Grinten, M. Wolff, H. Zabel, and A. Magerl, Meas. Sci. Technol. **19** (2008).
36. S. M. Baker, G. S. Smith, D. L. Anastassopoulos, C. Toprakcioglu, A. A. Vradis, and D. G. Bucknall, Macromolecules **33**, 1120 (2000).
37. R. Ivkov, P. D. Butler, and S. K. Satija, Langmuir **17**, 2999 (2001).
38. M. Walz, S. Gerth, P. Falus, M. Klimczak, T. H. Metzger, and A. Magerl, J. Phys.-Condens, Mat. **23** (2011).
39. M. Kawecki, P. Gutfreund, F. A. Adlmann, E. Lindholm, S. Longeville, and A. Lapp, et al., Journal of Physics: Conference Series **746**, 12014 (2016).
40. Z. Wen and J. Petera, Chemical and Process Engineering. **38**, 265 (2017).
41. M. M. de Beer, J. T. F. Keurentjes, J. C. Schouten, and J. van der Schaaf, Chem. Eng. J. **242**, 53 (2014).
42. K. S. Mriziq, H. J. Dai, M. D. Dadmun, G. E. Jellison, and H. D. Cochran, Rev. Sci. Instrum. **75**, 2171 (2004).
43. R. W. Connelly and J. Greener, J. Rheol. **29**, 209 (1985).
44. M. Özkan, P. J. Thomas, A. J. Cooper, and S. J. Garrett, Eng. Appl. Comp. Fluid **11**, 142 (2017).
45. S. Poncet, *Instabilities, Turbulence and Heat Transfer in Confined Rotating Flows*, Aix-Marseille Université (2014).
46. Z. Jiang and W. Chen, J. Appl. Crystallogr. **50**, 1653 (2017).
47. A. Korolkovas, P. Gutfreund, A. Chenneviere, J. F. Ankner, F. A. Adlmann, and M. Wolff, et al., Phys. Rev. E **98**, (2018).
48. R. Ivkov, P. D. Butler, S. K. Satija, and L. J. Fetters, Langmuir **17**, 2999 (2001).
49. J. Klein, D. Perahia, and S. Warburg, Nature **352**, 143 (1991).
50. J. Yu, N. E. Jackson, X. Xu, Y. Morgenstern, Y. Kaufman, and M. Ruths, et al., Science **360**, 1434 (2018).
51. Z. Zhang, A. J. Morse, S. P. Armes, A. L. Lewis, M. Geoghegan, and G. J. Leggett, Langmuir **27**, 2514 (2011).